# Tomography of integrated circuit interconnect with an electromigration void

Zachary H. Levine[a] and Andrew R. Kalukin[b]
*National Institute of Standards and Technology, Gaithersburg, Maryland 20899-8410 and Rensselaer Polytechnic Institute, Troy, New York 12180-3590*

Markus Kuhn
*Intel Corporation RA1-329, 5200 Northeast Elam Young Parkway, Hillsboro, Oregon 74124*

Sean P. Frigo, Ian McNulty, Cornelia C. Retsch, and Yuxin Wang
*Advanced Photon Source, Argonne National Laboratory, 9700 South Cass Avenue, Argonne, Illinois 60439*

Uwe Arp, Thomas B. Lucatorto, Bruce D. Ravel, and Charles Tarrio
*National Institute of Standards and Technology, Gaithersburg, Maryland 20899-8410*

(Received 29 September 1999; accepted for publication 19 January 2000)

An integrated circuit interconnect was subject to accelerated-life test conditions to induce an electromigration void. The silicon substrate was removed, leaving only the interconnect test structure encased in silica. We imaged the sample with 1750 eV photons using the 2-ID-B scanning transmission x-ray microscope at the Advanced Photon Source, a third-generation synchrotron facility. Fourteen views through the sample were obtained over a 170° range of angles (with a 40° gap) about a single rotation axis. Two sampled regions were selected for three-dimensional reconstruction: one of the ragged end of a wire depleted by the void, the other of the adjacent interlevel connection (or ''via''). We applied two reconstruction techniques: the simultaneous iterative reconstruction technique and a Bayesian reconstruction technique, the generalized Gaussian Markov random field method. The stated uncertainties are total, with one standard deviation, which resolved the sample to $200 \pm 70$ and $140 \pm 30$ nm, respectively. The tungsten via is distinguished from the aluminum wire by higher absorption. Within the void, the aluminum is entirely depleted from under the tungsten via. The reconstructed data show the applicability of this technique to three-dimensional imaging of buried defects in submicrometer structures relevant to the microelectronics industry. © *2000 American Institute of Physics.* [S0021-8979(00)00509-0]

## I. INTRODUCTION

Integrated circuit interconnects are three-dimensional structures of considerable complexity. Three-dimensional images of integrated circuits are of potential interest both to process development and to failure analysis groups within the semiconductor industry. X-ray tomography offers three-dimensional imaging with better resolution than optical microscopy and the ability to view optically hidden structures, and is less invasive than the thinning required for transmission electron microscopy (TEM). Here, we demonstrate the ability to image a typical failure in an integrated circuit, one induced in an accelerated life test used to generate an electromigration void. The sample was not specifically prepared for this experiment, but rather, taken from an inventory of samples prepared as part of a test suite by a semiconductor manufacturer.

Previously we imaged tomographically an integrated circuit interconnect without a void.[1] In this work, improvements in the hardware and software permitted a threefold improvement in spatial resolution compared to that in the previous experiment. Submicron x-ray tomography has been reported for samples other than integrated circuit interconnects[2–4] while nanometer-scale resolution had been obtained with tomography based on TEM.[5] However, this method is best suited to samples less than 1 $\mu$m in diameter. Because failures in integrated circuits are typically localized to a few $\mu$m at best, TEM alone may not be adequate to identify such a failure for imaging.

## II. EXPERIMENT

The formation of voids in integrated circuit interconnects is a major reliability concern. Accelerated life testing is used to induce electromigration voids which are similar to those encountered under normal operating conditions.[6] Our sample was taken from a test suite of electromigration-voided samples prepared by the Digital Equipment Corporation, Hudson, MA, that were made using technology producing a critical dimension of 0.35 $\mu$m for the transistor level. It consists of a two-level aluminum metallization stack (Ti/Al/Ti/TiN) joined by a tungsten interconnect or via. The interconnect lines are scaled to the critical dimension times a factor of 2 or more. This particular electromigration sample was prepared by maintaining a 2.3 mA current and a temperature of 220 °C for 300 h. Failure was determined by a pre-defined increase in resistance. These conditions are typical of accelerated life testing.[6] Although a void was formed in the interconnect, it still had electrical continuity because the Ti or TiN barrier layers or both were still intact. A nor-

[a]Electronic mail: zlevine@nist.gov
[b]Present address: Science Applications International Corporation, 4001 N. Fairfax Dr., Suite 300, Arlington, VA 22203.

 

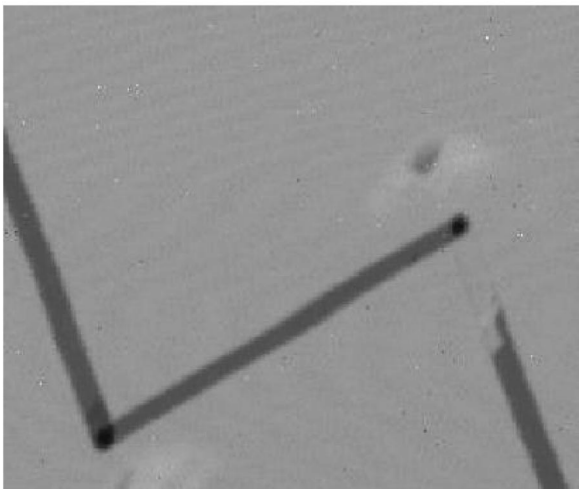

FIG. 1. Normal incidence projection of an integrated circuit interconnect with an electromigration void, imaged with $301\times301$ pixels with 57 nm step size and the 100 nm zone plate. The total field of view is 17.1 $\mu$m. The dark marks at the intersection of aluminum metallization are the tungsten vias, which join two different levels. The light regions near the vias are the remnants of focused ion beam markers which fell out during sample preparation.

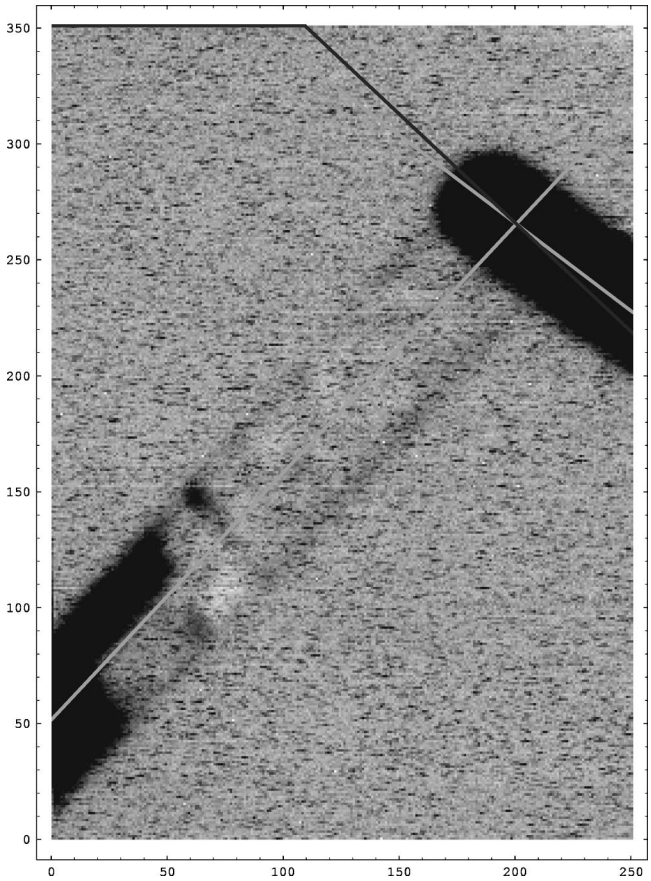


FIG. 2. Near-normal incidence projection of the same circuit imaged with $251\times351$ pixels with $20\pm3$ nm step size and the 45 nm zone plate. The scale is given in pixels. The total width is 250 pixels which corresponds to $5\pm0.75$ $\mu$m. The angle between the lines in the upper region indicate the distortion caused by the nonorthogonality of the scan stage. The broken interconnect end region is in the lower left corner. The via is under the aluminum which ends in the upper right corner, i.e., at the intersection of the two centerlines.

mal view optical micrograph did not show the presence of the underlying electromigration void because the barrier remained.

To prepare the sample for the experiment, the silicon substrate was removed entirely under the region of interest using techniques principally intended for the preparation of samples for TEM. However, the interconnect with its silica matrix was left intact; the sample was about 10 $\mu$m thick near the region of interest. The sample was then mounted onto a 3 mm diam Mo ring. The ring was, in turn, mounted onto the end of small rod and resembled a lollipop.

The tomographic projection data were collected with the scanning transmission x-ray microscope at the 2-ID-B beamline at the Advanced Photon Source.[7,8] The sample was scanned in two separate experimental runs. In the first run, the setup was essentially identical to that used previously;[1] the sample was imaged with $1573.0\pm1.5$ eV photons and a Fresnel zone plate with an outer zone width of 100 nm. The transverse imaging resolution of 150 nm using this zone plate, determined by a knife edge measurement,[8] is near the Rayleigh diffraction limit.[9] Throughout this article we give total uncertainties with one standard deviation. The sample was scanned in 57 nm steps with $301\times301$ pixels per projection. Projections were obtained at 12 angles, specifically, 0°, $\pm13.8°$, $\pm20.8°$, $\pm41.5°$, $\pm55.4°$, $\pm69.2°$, and $-76.2°$ from normal incidence. (All of these figures are subject to an uncertainty of 2° in a constant offset which does not affect the reconstruction.) The normal incidence projection is shown in Fig. 1. Two vias, a linking interconnect, and the electromigration void are clearly distinguishable.

In the second run, we used $1750.0\pm1.5$ eV photons, a zone plate with a 45 nm outermost zone width, and a motorized rotation stage with improved angular precision and runout. The larger photon energy was chosen to increase the transmission through the denser regions of the sample and to improve the signal-to-noise ratio at the largest angles. The sample was scanned in 20 nm steps with $251\times351$ pixels per projection at 14 angles over a 170° range, specifically, 2°, 12°, 32°, 42°, 57°, 62°, 72°, 112°, 122°, 132°, 142°, 152°, 162°, and 172° from normal incidence. The projection from near-normal incidence (2°) is shown in Fig. 2, showing one via and the electromigration void. Observations could not be made between 72° and 112° because the sample is planar and hence the distance the x rays travel through the sample becomes extremely large, leading to an insufficient signal. The minimum number of counts per pixel improved from 44 in the previous experiment to 148 without changing the sampling time.

The set of angles sampled is sparse, i.e., to reach the Nyquist sampling limit requires $\pi/2$ times the number of horizontal samples,[10] or 394 in this case. The undersampling is somewhat ameliorated by segmenting the image into regions 90 and 144 in width (see below), but these still require 141 and 226 angles to reach the Nyquist limit, i.e., at least an order of magnitude more than we obtained. As a consequence, there is no possibility that the three-dimensional (3D) resolution will be as fine as the two-dimensional (2D) resolution.

We estimated the transverse resolution in these projections by treating the interconnect as a knife edge. The Rayleigh criterion for resolution is interpreted here as meaning the distance required for a change in the transmitted intensity by a factor of 0.735.[11] A change by this factor occurs in $2.5\pm0.3$ pixels or $50\pm10$ nm, which is consistent with the 55 nm diffraction limit of the 45 nm zone plate according to the Rayleigh criterion. The width of the line shown in Fig. 2 is $1.1\pm0.2$ $\mu$m, which is consistent with the design rule that it is two or more times larger than the critical dimension of 0.35 $\mu$m.

The longitudinal resolution (depth of field) in each projection was 62 $\mu$m using the 100 nm zone plate at 1573 eV and 14 $\mu$m using the 45 nm zone plate at 1750 eV according to the Rayleigh criterion. In both cases, the depth of field is large compared to the sample thickness. However, the transverse resolution is modestly degraded for the high angles because the scanning stage moves transverse to the beam direction. Assuming the center of the sample is perfectly focused, the edge of the sample will be displaced from the focal plane by a half width of the sample times the sine of the viewing angle, or a maximum of 8.6 and 2.3 $\mu$m, which is still within the depth of field. This small effect is neglected in subsequent analysis, which relies on the straight-ray approximation.

The contrast of the 2D images is defined here as $(I_{\max}-I_{\min})/I_{\max}$, where $I_{\max}$ and $I_{\min}$ are local averages of the maximum and minimum intensities in the regions of greatest and least transmission. The maximum intensity corresponds to the regions of the sample with no metal. In the first data set, the contrast increases from 0.6 to 0.8 as the angle increases from 0° (normal incidence) to 69° in a region of a single aluminum wire, and up to 0.95 where two aluminum wires are present at 69°. The via region has a contrast of 1.0 at normal incidence, which declines to 0.8 at 69°. The contrast increases from 0.4 to 0.6 as the angle increases from 2° to 72° in the region of the aluminum wire, but decreases from 0.9 to 0.4 in the region of the tungsten via over this range. For the via region, at high angles, the x rays need only penetrate the via itself and not the aluminum above it; moreover, the tungsten via is higher than it is wide. This excessive contrast in the via region in the first run helps motivate the change in photon energy from 1573 to 1750 eV between the two experimental runs.

## III. RECONSTRUCTION

### A. Preprocessing

In the first run, we observed that the distance between fiducial references did not vary as expected as the cosine of the incidence angle. This indicated a systematic scale error in the projections, which we corrected for approximately by adjusting the horizontal ($x$) scale by a few percent in every projection to impose the cosine variation. After alignment to fiducial markers using the earlier method,[1] $250\times236$ pixel projection was available for reconstruction.

In the second run, we corrected distortion in the projections due to $x$- and $y$-axis coupling in the sample scan stage; here, $y$ is the vertical direction which is the rotation axis, $z$ is the beam direction, and $x$ completes a right-handed triad. To correct the coupling, it was necessary to fit the observed projections to a model which included three degrees of freedom for the orientation of the sample in space and three other degrees of freedom for the $x$ and $y$ coupling.[12] The fitting procedure rests on two assumptions: (a) the sample contains an orthogonal triad of unit vectors defined by the two interconnect levels and the via, and (b) the sample rotation axis is orthogonal to the beam direction. The three degrees of freedom for the $x$ and $y$ coupling are derived from a general $2\times2$ matrix with a fixed scale. Our fitting procedure was sensitive only to orientations of the chosen fiducials (i.e., the interconnect end via centerlines), not to their size. However, because the values in the coupling matrix differed from their ideal values (1 or 0) by an average of 0.15, the absolute scale is uncertain at this level, i.e., 15%, as well. From the fit, we also learned that the sample normal was offset from the beam direction by 2° after initial alignment.

A two-dimensional scan is presented in Fig. 2. The electromigration voided region may be seen in this projection; additional detail is present compared with Fig. 1. The solid lines illustrate the apparent nonorthogonality of the lines in the sample due to $xy$ coupling in the scan stage. The matrix describing the coupling of the $x$ and $y$ motion was obtained, then the inverse of this matrix was applied to all of the projections to remove the effect of the $x$ and $y$ coupling of the stage motion. The description below refers to operations on the uncoupled projections.

Before the samples can be reconstructed, they must be aligned. We opted to use fiducial marks intrinsic to the sample for this procedure. In our case the prominent features are the two aluminum interconnects and the tungsten via. The centerlines of the three features were determined by finding visible boundary points by hand with the aid of a graphical display program, and taking the centerline as the average of the edge lines. The intersections of the three lines as seen in the projection at each viewing angle were calculated as a function of the height of the via. The intersections of the various lines are proportional to the height of the via and, working backwards, the height of the interlayer spacing was determined. It was $92.4\pm1.3$ pixel or $1850\pm280$ nm. This size is typical of integrated circuit interlayer spacings. For example, the Advanced Micro Devices (AMD) K6 chip has an aluminum metallization interconnect structure including tungsten vias with an average interlayer spacing of 2.0 $\mu$m.[13]

Additionally, we averaged adjacent rows when data were missing (two rows in the entire data set) and data that differed from the average of the adjacent pixels by more than 10 standard deviations were replaced by the average; this situation occurred for a few pixels per 10 000.

### B. Simultaneous iterative reconstruction technique reconstruction

For the first run, we used the simultaneous iterative reconstruction technique (SIRT) method.[1] The results are shown in Fig. 3. The three-dimensional character of the interconnect is obtained in this reconstruction, but the noise

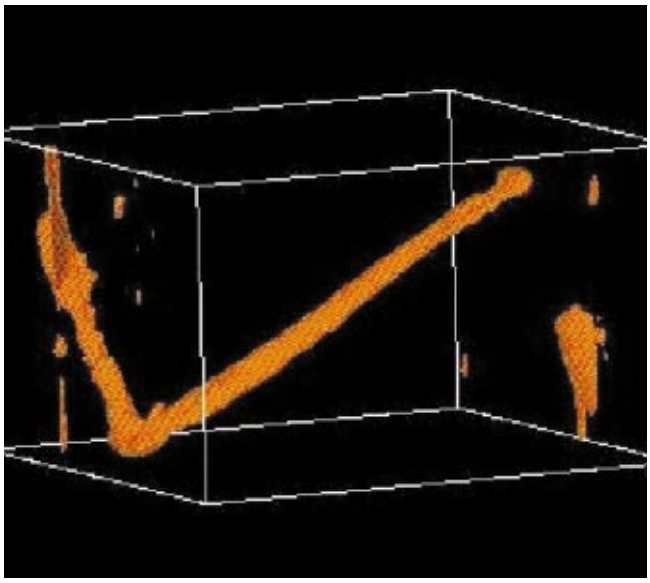

FIG. 3. (Color) Three-dimensional SIRT reconstruction of the sample measured with coarse resolution with parameters as in Fig. 1. The electromigration void is the gap between the two major orange regions on the right side.

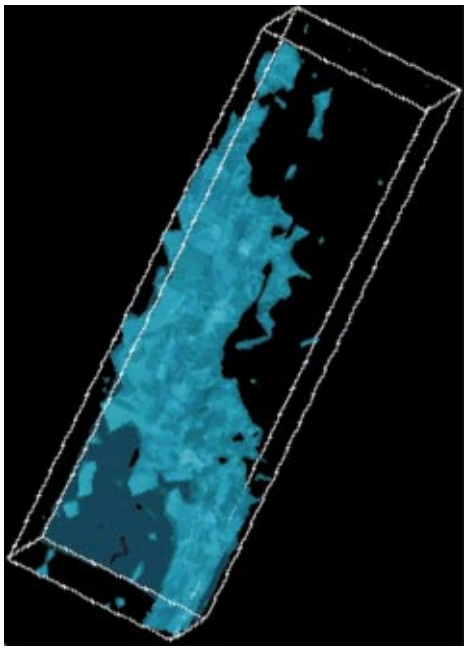

FIG. 4. (Color) Three-dimensional SIRT reconstruction of the aluminum end region of the sample measured with finer resolution (same parameters as in Fig. 2). This region is associated with the remaining aluminum in the lower left corner of Fig. 2 and equivalently the large orange metal region in the lower right portion of Fig. 3.

level is high enough that little more may be learned about the voided region which is not already evident in the normal incidence projection (Fig. 1).

The two interesting regions in the sample are the beginning and the end of the electromigration voided region. For the second experiment, we chose to reconstruct these data sets separately to reduce the size of the regions to be reconstructed. It was important to minimize this size so that the reconstruction would depend only on the measured data and not regions far to the side of what was measured. As a side benefit, the time of the reconstructions fell by a factor of about 4. In practice, it was necessary to copy a couple of small background regions from adjacent areas to fill out the required input to the reconstruction programs. The aluminum end was reconstructed in an oblique cylinder 90 pixels in diameter and 150 pixels high, centered on the interconnect. In the oblique cylinder, the width of the reconstructed region did not depend on the height $y$, but the center $X$ and $Z$ positions ($X$ and $Z$ being coordinates in three dimensions) were linearly dependent on $y$. This led to a sinusoidally varying shift in the projection $x$ coordinates to ensure correct alignment in three dimensions, because $x = X\cos\theta + Z\sin\theta$ for viewing angle $\theta$. The via was reconstructed in a region of $144 \times 100$ pixels aligned with the $y$ axis.

The SIRT technique was applied successfully to the aluminum end region. The result, after the removal of a ring artifact toward the outside of the region, is shown in Fig. 4. The isosurface which is most representative of the edge of the sample is presented. The half-line structure seen in Fig. 1 is present in the projection from the three-dimensional reconstruction as well. However, some island features appear in the image which are almost certainly not real. Unfortunately, the SIRT code did not produce a recognizable image of the via region.

### C. Bayesian reconstruction

In practice, the image reconstruction problem is underconstrained because we have several times more degrees of freedom in the image than the number of observations. Hence, it is necessary to make assumptions. The SIRT algorithm makes assumptions about the unconstrained data implicitly: it never modifies any linear combination of the data which does not affect a constraint equation.[14] If one starts, as we do, from an initial guess of 0, this is equivalent to assuming a 0 value for the missing data.

Under a Bayesian method, the reconstructed image depends both upon the measured data and explicit assumptions about the missing data. Bouman and Sauer introduced a Bayesian method called the generalized Gaussian Markov random field (GGMRF) method,[15] in part to handle abrupt changes in density in materials inspection problems in tomography, while retaining much of the analytic simplicity of the earlier Gaussian Markov random field (GMRF) method. The materials inspection problem is characterized by the presence of a few edges, i.e., discontinuous changes in the density of the material. The discontinuous changes tend to be blurred or noisy under GMRF but better reconstructed under the GGMRF, which does not penalize them as severely.[15] GMRF does well when the density to be reconstructed varies continuously. Under the GGMRF, one weights the likelihood of any image in the solution space $X$ with a sum over nearest neighbors of $|X_s - X_{s+r}|^p$, where $s$ is a (2D) index which runs over the image, $r$ is an image offset to describe the nearest neighbor sum, and $1 \leqslant p \leqslant 2; p = 2$ is the GMRF case. The $p = 1$ case has the property that any monotonic change from one density value to another has the same likelihood,

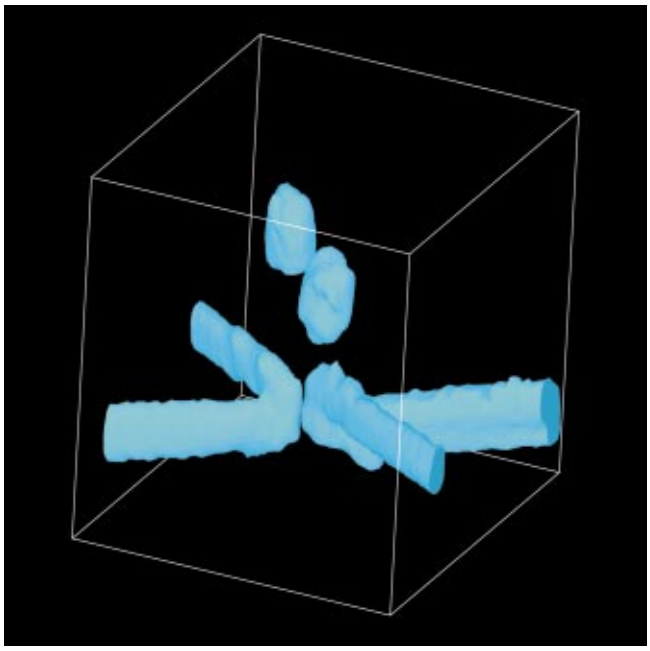

FIG. 5. (Color) Bayesian reconstruction of an integrated circuit interconnect using same data as in Ref. 1. The distance from the plane of the balls (focused ion beam markers) to the center of the upper interconnect line is $5.4 \pm 0.5\ \mu$m.

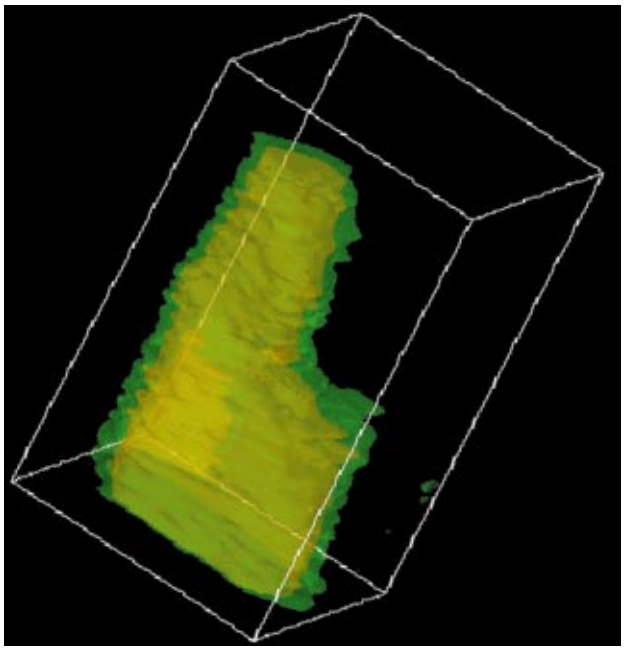

FIG. 6. (Color) Bayesian reconstruction of the ragged end of the aluminum shown in Figs. 1 and 2. The reconstruction was performed on the same data as in Fig. 4.

but any nonmonotonic change is less favored; for larger $p$, the more gradual changes are favored.

The Bayesian algorithm was applied to the projection data of an integrated circuit interconnect acquired earlier.[1] No additional preprocessing was done. Reconstructions of selected slices were performed with $p$ set to 2, 1.4, 1.2, 1.1, and 1.05. The values of 2 and 1.4 softened the edges unreasonably, but the values of 1.2, 1.1, and 1.05 were all very similar and plausible. This result is in accordance with expectation.[15] A full reconstruction was performed with $p = 1.1$; a view is presented in Fig. 5. The image is much smoother than the SIRT reconstructions presented in Figs. 3–5 of Ref. 1, and more in accord with the projections (Figs. 1 and 2 of Ref. 1) which show straight edges. The roughness of those earlier SIRT reconstructions was used to estimate its spatial resolution at 400 nm. Here, an estimate is made based on the distance for a change in value of by a factor of 0.735 when an abrupt change is expected. This is found to be $3.6 \pm 1.0$ pixel. As in Ref. 1, the pixel size is $57 \pm 5.7$ nm, leading to a measured resolution of $200 \pm 70$ nm, i.e., about twice as good.

Similarly, the Bayesian method was applied to the circuit with the electromigration void. For the coarse resolution data, we failed to obtain a reconstruction with this method, despite the successful reconstruction of SIRT illustrated in Fig. 3. For the fine resolution data, reconstructions were obtained without further preprocessing. The region of the wire end is shown in Fig. 6. The resolution is estimated as above to be $7 \pm 1$ pixel, or $140 \pm 30$ nm. This is comparable to a resolution of $10 \pm 3$ pixel or $200 \pm 70$ nm for SIRT. The uncertainty in the resolution is higher for SIRT because the isosurfaces generated by SIRT are rougher than those by the Bayesian method. The relative resolution of the two methods is $0.7 \pm 0.2$, and is independent of the pixel size and its uncertainty.

The via region containing a void is shown in Fig. 7. Two isosurfaces are shown, one at twice the density of the other. The high density isosurface is coincident with the tungsten via; the low density isosurface is primarily coincident with the aluminum wire, although the continuity of the density

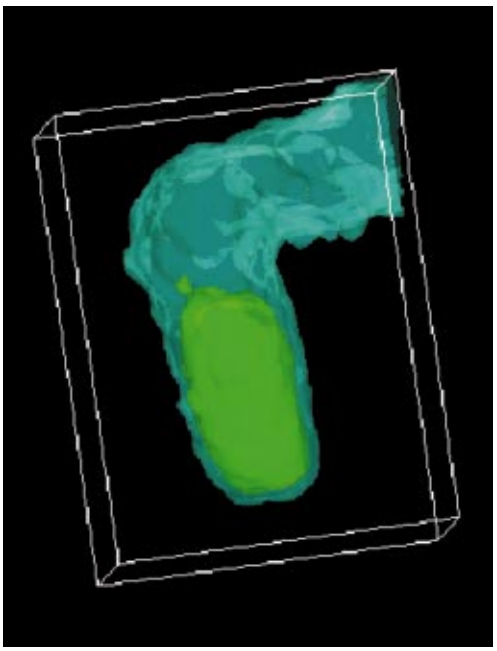

FIG. 7. (Color) Bayesian reconstruction of the interconnect shown in Figs. 1 and 2. The density represented by the green isosurface is twice that of the blue isosurface. The green region is coincident with the expected location of the W via. Had the circuit not had the electromigration void, a blue surface would be attached to both ends of the via, like in Fig. 5.

imposes a low density isosurface in the tungsten region as well. In this sense, the materials are not uniquely identified by the isosurfaces. The aluminum under the via is largely or entirely swept away. This result is consistent with expectation.[6]

## IV. CONCLUSION

We have imaged two integrated circuit interconnects, one with and one without an electromigration void, and employed two reconstruction algorithms, the simultaneous iterative reconstruction technique and the generalized Gaussian Markov random field, a Bayesian technique. The GGMRF was developed specifically for materials inspection problems which are characterized by abrupt changes in density. The Bayesian technique was superior, leading to a factor of 2 better resolution in three dimensions as well as avoiding a ring artifact. A resolution of $140 \pm 30$ nm in three dimensions was achieved in the best case.

Present day integrated circuits in production have 180 nm linewidths; 130 nm is anticipated by the year 2003.[16] One requires a resolution of 70 nm (and shortly 50 nm) or better to perform failure analysis at the level needed to identify critical defects in production circuits. One may hope to achieve this factor-of-three gain through a combination of improved Fresnel zone plates, leading to a smaller two-dimensional resolution, as well as better sampling and alignment to reduce the loss from two-dimensional to three-dimensional resolution—presently a factor of 3—which appears in practice, but not in theory.[17]

## ACKNOWLEDGMENTS

The authors acknowledge funding provided by the Semiconductor Research Corporation, the Advanced Technology Program at the National Institute of Standards and Technology, and the Department of Energy, Basic Energy Sciences, Office of Energy Research, under Contract No. W-31-109-ENG-38. The samples were fabricated by Steven Bill at the former Digital Equipment Corporation. The zone plates were fabricated in collaboration with Erik Anderson and Wenbing Yun of the Lawrence Berkeley Laboratory. The SIRT reconstruction code was written by Steve Lamont of the University of California at San Diego; the Bayesian reconstruction code was written by Charles Bouman, Purdue University, and collaborators. Computer assistance was provided by Terence Griffin and Matt Loebach of NIST. Helpful discussions with Wayne Roberge of Rensselaer Polytechnic Institute are acknowledged. The authors are grateful for the critical support from these many people and organizations. Certain commercial equipment, instruments, or materials are identified in this article to foster understanding. Such identification does not imply recommendation or endorsement by the authors' institutions nor does it imply that the materials or equipment identified are necessarily the best available for the purpose.

[1] Z. H. Levine, A. R. Kalukin, S. P. Frigo, I. McNulty, and M. Kuhn, Appl. Phys. Lett. **74**, 150 (1999).
[2] W. S. Haddad, I. McNulty, J. E. Trebes, E. H. Anderson, R. A. Levesque, and L. Yang, Science **266**, 1213 (1994).
[3] J. Lehr, Optik (Stuttgart) **104**, 166 (1997).
[4] A. R. Kalukin, B. Winn, Y. Wang, C. Jacobsen, Z. H. Levine, and J. Fu, J. Res. Natl. Inst. Stand. Technol. (in press).
[5] B. F. McEwen and A. B. Heagle, Int. J. Imaging Syst. Technol. **8**, 175 (1997).
[6] C.-K. Hu, K. P. Rodbell, T. D. Sullivan, K. Y. Lee, and D. P. Bouldin, IBM J. Res. Dev. **39**, 465 (1995).
[7] I. McNulty, A. M. Khounsary, Y. P. Feng, Y. Qian, J. Barraza, C. Benson, and D. Shu, Rev. Sci. Instrum. **67**, 9 (1996), CD-ROM.
[8] I. McNulty, Y. P. Feng, S. P. Frigo, and T. M. Mooney, Proc. SPIE **3150**, 195 (1997).
[9] J. Kirz, C. Jacobsen, and M. Howells, Q. Rev. Biophys. **28**, 33 (1995).
[10] B. P. Flannery, H. W. Deckman, W. G. Roberge, and K. L. D'Amico, Science **237**, 1439 (1987).
[11] M. Born and E. Wolf, *Principles of Optics*, 5th Ed., (Pergamon, New York, 1975), p. 415, Sect. 8.6.2.
[12] A. R. Kalukin, Z. H. Levine, C. Tarrio, S. P. Frigo, I. McNulty, Y. Wang, C. C. Retsch, M. Kuhn, and B. Winn, Proc. SPIE **3772**, 237 (1999). After the experiment was completed, we determined a simpler method for removing linear distortion which may be performed by imaging any two orthogonal lines such as those found on a grid at just two viewing angles, 0° and 180°. Let $T$ be a $2\times2$ matrix describing the linear distortion of the stage, let $V$ be a pair of vectors measured at 0°, and let $W$ be a pair of vectors measured at 180°. The intrinsic vectors may be described by a $2\times2$ orthogonal matrix $M=\left(\begin{smallmatrix}\cos\theta & \sin\theta\\ -\sin\theta & \cos\theta\end{smallmatrix}\right)$. Then $V=TM$ and $W=T\sigma_X M$, where $\sigma_X=\left(\begin{smallmatrix}-1 & 0\\ 0 & 1\end{smallmatrix}\right)$. Then $\theta$, and hence $M$, may be determined from $V^{-1}W=M^{-1}\sigma_X M=\left(\begin{smallmatrix}\cos 2\theta & 0\\ 0 & \cos 2\theta\end{smallmatrix}\right)$. Finally, $T$ may be found from $VM^{-1}$.
[13] I. C. E. Laboratories, AMD's K6 Microprocessor, poster, 1998.
[14] K. M. Hanson and G. W. Wec kung, J. Opt. Soc. Am. **73**, 1501 (1983).
[15] C. Bouman and K. Sauer, IEEE Trans. Image Process. **2**, 296 (1993); the source was obtained from http://dynamo.ecn.purdue.edu/~bouman/software/tomography, under tomo_pack.tar.Z, program FR.
[16] Semiconductor Industry Association, *National Technology Roadmap for Semiconductors* (SEMATECH, San Jose, CA, 1997), http://notes.sematech.org/ntrs/PublNTRS.nsf.
[17] F. Natterer, *The Mathematices of Computerized Tomography* (Wiley and Teubner, Stuttgart, 1986), pp. 68–69.